Sb-Based Alloy (NiSb, FeSb$_2$) Nanoparticles Decorated Graphene Prepared by One-Step Solvothermal Route as Anode for Li-Ion Batteries

Jian Xie[*], *Yun-Xiao Zheng, Rui-Jun Pan, Shuang-Yu Liu, Wen-Tao Song, Gao-Shao Cao, Tie-Jun Zhu, and Xin-Bing Zhao*

Department of Materials Science and Engineering, Zhejiang University, Hangzhou 310027, China
[*]E-mail: xiejian1977@zju.edu.cn

NiSb/graphene and FeSb$_2$/graphene nanocomposites were fabricated by a facile one-step solvothermal route using graphite oxide, NiCl$_2$·2H$_2$O (or FeCl$_3$·6H$_2$O) and SbCl$_3$ as the starting materials and NaBH$_4$ as the reductant. NiSb (20-30 nm) and FeSb$_2$ (around 5 nm) nanoparticles were uniformly dispersed and confined by the graphene sheets, forming a unique hybrid nanostructure. The electrochemical properties of the nanocomposite were investigated by galvanostatic cycling, cyclic voltammetry and electrochemical impedance spectroscopy. The nanocomposites exhibit an obviously enhanced electrochemical performance compared with bare alloys. The improvement in the electrochemical performance could be attributed to the introduction of graphene that constructs a two-dimensional conductive network, uniformly disperses and confines the alloy particles and effectively buffers the volume changes.

1. INTRODUCTION

Rechargeable Li-ion batteries are currently prevailing power sources for mobile electronic devices and show potential applications in electric vehicles (EVs). Carbon-based materials are now widely used as the anodes for commercial Li-ion batteries because of the low cost, good cycling stability and appropriate Li-storage potential. In recent years, great interest has been turned to some Sb-based materials [1−12] to replace the conversional carbon materials in order to meet the ever increasing high-energy-density requirement for Li-ion batteries. Although Sb-based materials have a high theoretical capacity by forming a Li$_3$Sb composition, they show rapid capacity fade due to large volume changes upon Li-absorption/extraction.

Great effort has been made to alleviate the volume changes to improve the cycling stability of the Sb-based materials. Thin-film materials [13−15] are suitable candidates since they have an extremely large surface/volume ratio that is favorable to reduce the stress caused by volume changes. For instance, Sb_2O_3 thin film exhibited a good cycling stability up to 70 cycles without capacity fading [16]. Nanostructured materials are also considered as promising candidates because of their small particle size and fast Li-ion diffusion which brings reduced absolute volume changes [17−21]. Our previous work showed that some nanosized Sb-based anodes exhibited an improved electrochemical stability than their microsized counterparts [22−24]. Another attractive method to relief volume changes is to form composites with other materials. Carbon materials, such as carbon nanotubes [25, 26], amorphous carbon [27, 28], and carbon [29, 30] have been used as matrices to buffer the volume changes of the Sb-based materials due to their flexibility. In addition, they also contribute to the overall capacity and increase the electric conductivity of the composites.

Graphene, a flat monolayer of sp^2-bonded carbon atoms arranged in a tightly packed honeycomb two-dimensional (2D) lattice, has attracted a considerable interest since first discovered by K. S. Novoselov group in 2004 [31]. The combined merits of the high electronic conductivity [32], high specific surface area [33] and high mechanical strength [34] make graphene a promising 2D support for nanostructured anode materials. Recent researches on some metals [35−38] or oxides [39−42] with a Li-alloying/de-alloying Li-storage mechanism, have showed that the electrochemical performance of these materials can be remarkably enhanced by loading them onto graphene sheets. Herein, we report a facile preparation of NiSb/graphene and $FeSb_2$/graphene nanocomposites by an in situ one-step solvothermal route. The microstructure of the nanocomposites and the effect of graphene on the electrochemical properties will be discussed.

2. EXPERIMENT SECTION

2.1 Preparation of NiSb/graphene and FeSb₂/graphene nanocomposites

Graphite oxide (GO), which was prepared by a modified Hummer's method [43], was dispersed in 60 mL of absolute ethanol by ultrasonication for 3 h. Then, 2 mmol $NiCl_2·6H_2O$ (or 2 mmol $FeCl_3·6H_2O$ for $FeSb_2$) and 2 mmol $SbCl_3$ (4 mmol $SbCl_3$ for $FeSb_2$) were added to the above dispersion with ultrasonication for another 0.5 h, followed by adding sufficient $NaBH_4$ to reduce Ni^{2+} (or Fe^{3+}) and Sb^{3+}. The graphite-oxide/NiSb (or $FeSb_2$) weight ratio is 1:5. The mixture was transferred to a Teflon-lined stainless steel autoclave and maintained at 180 ºC (220 ºC for $FeSb_2$) for 24 h. The resulting products were separated by centrifugation, washed with deionized water and dried at 30 ºC under vacuum for 10 h. The obtained products are named as NiSb/G and $FeSb_2$/G, where G represents graphene. For comparison, bare NiSb and bare $FeSb_2$ were also prepared with the similar route without adding the graphite oxide during the synthesis.

2.2 Physicochemical characterization

The crystalline structure of the obtained products was characterized by X-ray diffraction (XRD) on a Rigaku D/Max-2550pc powder diffractometer equipped with Cu K_α radiation ($\lambda = 1.541$ Å). Raman spectra were collected on a Jobin-Yvon Labor Raman HR-800 Raman system by exciting a 514.5 nm Ar^+ laser. X-ray photoelectron spectroscopy (XPS) measurements were performed on a KRATOS AXIS ULTRA-DLD spectrometer with a monochromatic Al K_α radiation (*hv* = 1486.6 eV). The morphologies of the products were observed by field emission scanning electron microscopy (FE-SEM, FEI-sirion), transmission electron microscopy (TEM, JEM 2100F) and high-resolution TEM (HRTEM). The carbon content was measured on a Flash EA 1112 tester.

2.3 Electrochemical measurements

The electrochemical performance of the as-synthesized NiSb/G and $FeSb_2$/G was evaluated using CR2025-type coin cells. The electrode slurry was made by mixing 75 % wt NiSb/G (or $FeSb_2$/G), 15% wt acetylene black and 10 % wt polyvinylidene fluoride (PVDF) in N-methyl pyrrolidone (NMP) with magnetic stirring for 2 h. The slurry was then pasted onto Ni foam to make the working electrodes followed by drying at 100 °C under vacuum for 8 h. Cell assembly was carried out in an argon-filled glove box using metallic Li foil as the counter electrode, 1 M $LiPF_6$ in ethylene carbonate (EC)/dimethyl carbonate (DMC) (1:1 by volume) as the electrolyte, and polypropylene microporous film (Celgard 2300) as the separator. The cells were galvanostatically charged and discharged on a LHS-B-5V5mA8D battery cycler (Wuhan, China) in the voltage range of 0.05-1.5 V (vs. Li/Li$^+$) at 40 mA g^{-1}. Cyclic voltammetry (CV) measurements were performed on an Arbin BT2000 system between 0.05 and 2.0 V (vs. Li/Li$^+$) at a scan rate of 0.1 mV s^{-1}. Electrochemical impedance spectroscopy (EIS) measurements were carried out on a CHI660C electrochemistry workstation. The impedance plots were recorded by applying an AC signal of 5 mV amplitude over the frequency range from 10^5 Hz to 10 mHz at de-lithiation state. All the electrochemical measurements were conducted at 25 ºC.

3. RESULTS AND DISCUSSION

3.1 Characterization of NiSb/G nanocomposite

Fig. 1(a) shows the XRD patterns of the NiSb/G composite and bare NiSb. All the diffraction peaks can be indexed to hexagonal NiSb (space group *P6₃/mmc*, JCPDS No. 75-0604) for both NiSb/G and bare NiSb. No obvious peaks for graphene can be observed, suggesting that during the in situ preparation of the NiSb/G composite, the restacking of the reduced graphene oxide is restrained by uniformly loading NiSb particles in between the graphene sheets. The electrostatic attraction between the positively charged ions (Ni^{2+} and Sb^{3+}) and the negatively charged graphene oxide sheets [44] plays

a crucial role in the attachment of the NiSb particles on graphene. The amount of graphene in the composite is around 7% wt according to the carbon content analysis.
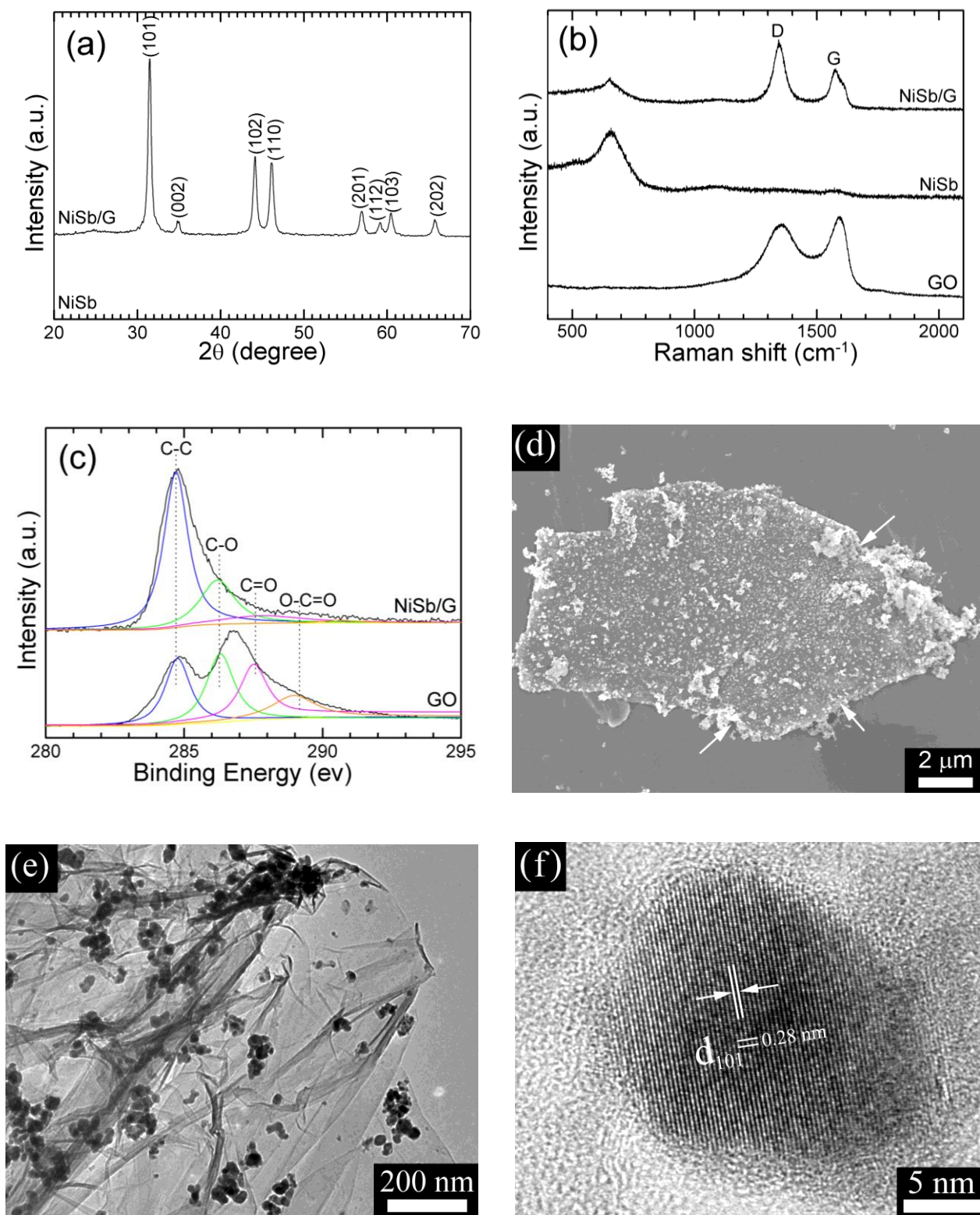
Figure 1. (a) XRD patterns of NiSb/G and bare NiSb, (b) Raman spectra of NiSb/G, bare NiSb and GO, (c) C 1s XPS of NiSb/G and GO, (d) SEM, (e) TEM and (f) HRTEM of NiSb/G.

Fig. 1(b) gives the Raman spectra of GO, NiSb/G, and bare NiSb. Two bands at 1350 and 1580 cm^{-1} appear in the Raman spectra of NiSb/graphene, corresponding to the disordered (D) band and graphitic (G) band of carbon materials. Compared with GO, the composite exhibits an increased D/G intensity ratio which is caused by a reduction of the average size of the sp^2 domains, signifying the conversion from GO to graphene [45]. The small peak at 650 cm^{-1} is related to the Raman active modes of Sb$_2$O$_3$ [46]. The degree of reduction of GO is further checked by XPS shown in Fig. 1(c). The XPS spectra can be deconvoluted into four peaks, corresponding to carbon atoms in different functional groups: sp^2 carbon (C-C, 284.7 eV), carbon in C-O bonds (286.1 eV), carbonyl carbon (C=O, 287.6 eV) and carboxylate carbon (O-C=O, 290.2 eV) [45, 47, 48]. Note that after the solvothermal reaction, the peak intensity for the non-sp2 carbon was remarkably reduced, indicating a sufficient reduction of GO.

Fig. 1(d) shows typical SEM images of a NiSb/G flake. From the surface morphology of flake, it is clear that the nanosized NiSb particles are attached on graphene. A sandwich structure with alternating NiSb-nanoparticles and graphene sheets is evident from the broken cross section of the flake. TEM observation (Fig. 1(e)) indicates that the NiSb particles with a size of 20-30 nm are uniformly anchored on graphene. The graphene is rather thin evidenced from its transparent nature and the surface wrinkles. Fig. 1(f) displays the lattice resolved HRTEM images of an individual NiSb particle on graphene. The fringe spacing is measured to be 0.28 nm, corresponding to the interplanar spacing of (101) plane of NiSb. Thus, it can be concluded from the XRD, Raman, XPS, SEM and TEM analyses that a NiSb/G nanocomposite has formed during the one-step solvothermal reaction.

3.2 Characterization of FeSb$_2$/G nanocomposite

Fig. 2(a) gives the XRD patterns of FeSb$_2$/G and bare FeSb$_2$ after the solvothermal reaction at 220 ºC. The dominant diffraction peaks can be indexed to orthorhombic FeSb$_2$ (space group *Pnn*2, JCPDS No. 71-2210) for both the samples. The absence of the graphene peaks also suggests that the graphene sheets are sufficiently exfoliated to form a FeSb$_2$/G layered structure. The graphene content is measured to be around 8% wt by the carbon content analysis. The Raman spectra (Fig. 2(b)) also indicate the conversion from GO to graphene during the solvothermal reaction based on the above analysis. Note that the intensity of the Raman peak related to the surface oxide in the composite is significantly reduced compared with that in bare FeSb$_2$, indicative of the suppressed surface oxidation of the FeSb$_2$ particles by confining them in between the graphene sheets. The XPS results further verifies the formation of graphene after the solvothermal reaction as shown in Fig. 2(c).

Fig. 2(d) displays the typical SEM images of a FeSb$_2$/G flake. From the inclined and broken cross sections of the flake (directed by the arrows), a layered structure constructed by alternating FeSb$_2$-nanoparticles and graphene sheets is evident, similar to the case for NiSb/G. TEM observation demonstrates that the transparent graphene is decorated homogeneously with small-sized FeSb$_2$ particles (Fig. 2(e)). HRTEM image shows that the particle size of FeSb$_2$ is around 5 nm as seen in Fig. 2(f), smaller than that of NiSb. In addition, it seems that the FeSb$_2$ particles exhibit a more

homogeneous dispersion than the NiSb particles. Based on the above analyses, we can conclude that a $FeSb_2/G$ nanocomposite has formed by this one-step solvothermal route.
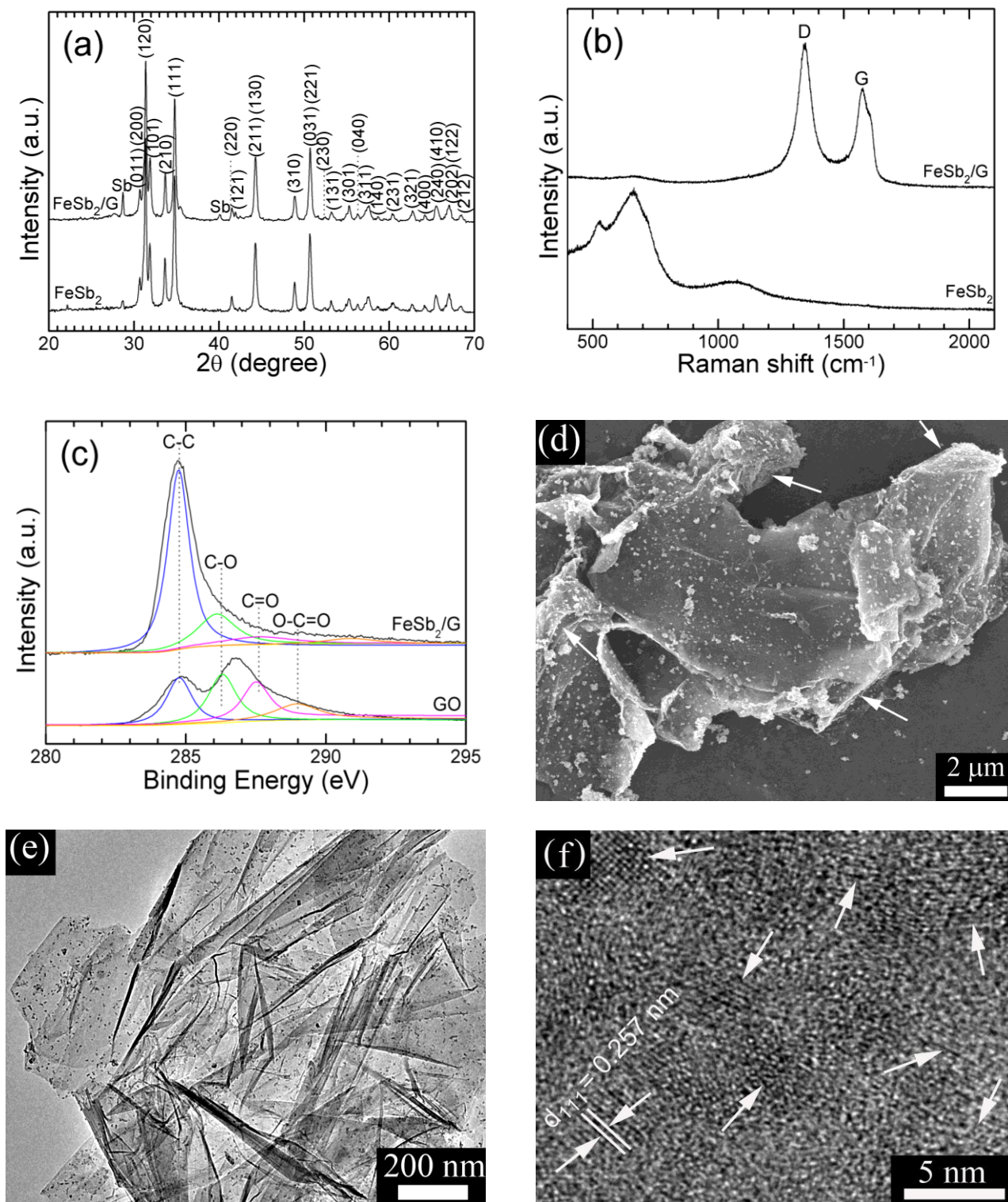
Figure 2. (a) XRD patterns of $FeSb_2/G$ and bare $FeSb_2$, (b) Raman spectra of $FeSb_2/G$ and bare $FeSb_2$, (c) C 1s XPS of $FeSb_2/G$ and GO, (d) SEM, (e) TEM and (f) HRTEM of $FeSb_2/G$.

3.3 Electrochemical properties of NiSb/G nanocomposite

Fig. 3(a) shows the chare-discharge curves of NiSb/G for the first three cycles. Note that the nanocomposite gives s a first discharge (Li-absorption) capacity of 855 mAh g^{-1} and a first charge capacity of 414 mAh g^{-1}. The large first irreversible capacity can be attributed to the reduction decomposition of the electrolyte and the formation of the solid state interface (SEI) layer. Furthermore, the surface oxide also contributes to part of the irreversible capacity.
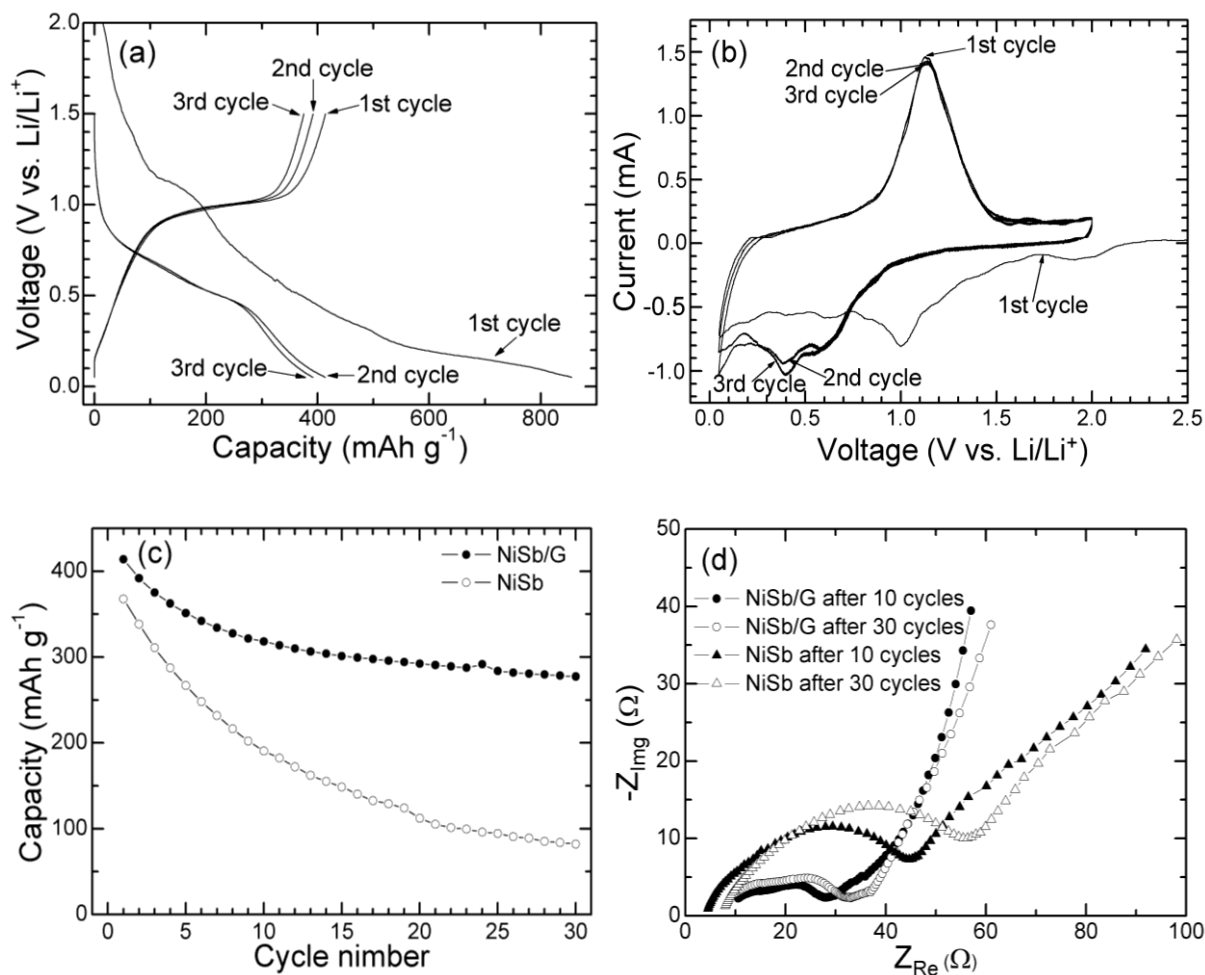
Figure 3. Charge-discharge curves (a) and CV (b) plots of NiSb/G, (c) comparison of cycling stability between NiSb/G and bare NiSb, and (d) Nyquist plots of NiSb/G and NiSb after different cycles.

After the first cycle, reversible electrochemical reactions take place evidenced by the almost overlapped charge or discharge curves. The electrochemical reaction mechanism of the nanocomposite was investigated by CV shown in Fig. 3(b).

During the first scan, a reduction peak appears at about 1.0 V, corresponding to the quasi-plateau in the first discharge curve, which is related to the formation of the SEI layer. After the first

scan, the reduction and oxidation peaks are fixed at around 0.4 and 1.0 V, respectively, suggesting a good reversibility during the subsequent cycling.

Fig. 3(c) compares the cycling stability between NiSb/G and bare NiSb. It is obvious that the nanocomposite exhibits an improved cycling stability compared to bare NiSb. After 30 cycles, a capacity close to 280 mAh g^{-1} is maintained for NiSb/G, while for bare NiSb, the capacity drops rapidly to 82 mAh g^{-1} after the same cycles. The enhanced cycling stability is attributed to the buffering effect of graphene that alleviates the large volume changes and the confinement effect of graphene that restrains the aggregation of the NiSb nanoparticles. In addition, the 2D conductive network constructed by graphene also contributes to the improved electrochemical performance by increasing the electronic conductivity of the composite and enhancing the electrochemical kinetics.

Fig. 3(d) compares the Nyquist plots of NiSb/G and bare NiSb after 10 and 30 cycles. The Nyquist plots consist of a depressed semicircle in the high-to-middle frequency region and a slopping line in the low frequency region.

As previously reported [49], the depressed semicircle corresponds to the charge transfer resistance (R_{ct}) across the electrode/electrolyte interface, the slopping line is related to the Li-ion diffusion in the bulk electrode, and the intercept on the Z_{Re} axis at high frequency is related to the electrolyte resistance.

Clearly, the NiSb/G electrode exhibits a smaller R_{ct} than the bare NiSb electrode. The smaller R_{ct} can be ascribed to the more uniform dispersion of the nanoparticles and better wetting of the active materials with the electrolyte by introducing graphene with a large specific surface area. Besides, the NiSb/G electrode shows a smaller increase of R_{ct} than the bare NiSb electrode during cycling due likely to the stabilized electrode/electrolyte interface by confining NiSb nanoparticles into the graphene sheets. The EIS tests agree well with electrochemical performance.

3.4 Electrochemical properties of FeSb$_2$/G nanocomposite

Fig. 4(a) shows the chare-discharge curves of FeSb$_2$/G for the first three cycles. The first charge capacity of FeSb$_2$/G is 446 mAh g^{-1}, slightly higher than that of NiSb/G. However, the FeSb$_2$/G electrode exhibits a larger first irreversible capacity than the NiSb/G electrode, possibly because of the smaller particle size.

The large specific surface area of the small particles facilitates the reduction decomposition of the electrolyte on their surface. The broad reduction peak at 1.0 V in Fig. 4(b) also indicates that the decomposition of the electrolyte and the formation of the SEI layer are profound for FeSb$_2$/G. After the first cycle, the FeSb$_2$/G electrode also exhibits reversible cycling as seen from the reproducible charge-discharge curves and CV plots.

It can be seen from Fig. 4(c) that the FeSb$_2$/G electrode shows a better cycling stability than the bare FeSb$_2$ electrode especially in the initial cycles. The buffering and confining effects of the introduced graphene plays a critical role in the improvement of the electrochemical performance. The Nyqusit plots of the FeSb$_2$/G and the bare FeSb$_2$ electrodes are also compared in Fig. 4(d). Again, the

$FeSb_2/G$ electrode shows a smaller R_{ct} values and a smaller change of R_{ct} than the bare $FeSb_2$ electrode, in agreement with the cycling results.

It should be stressed that the long-term cycling stability of both the $NiSb/G$ and $FeSb_2/G$ electrodes, however, is not satisfactory yet due to the intrinsic large volume changes of the Sb-based electrode.
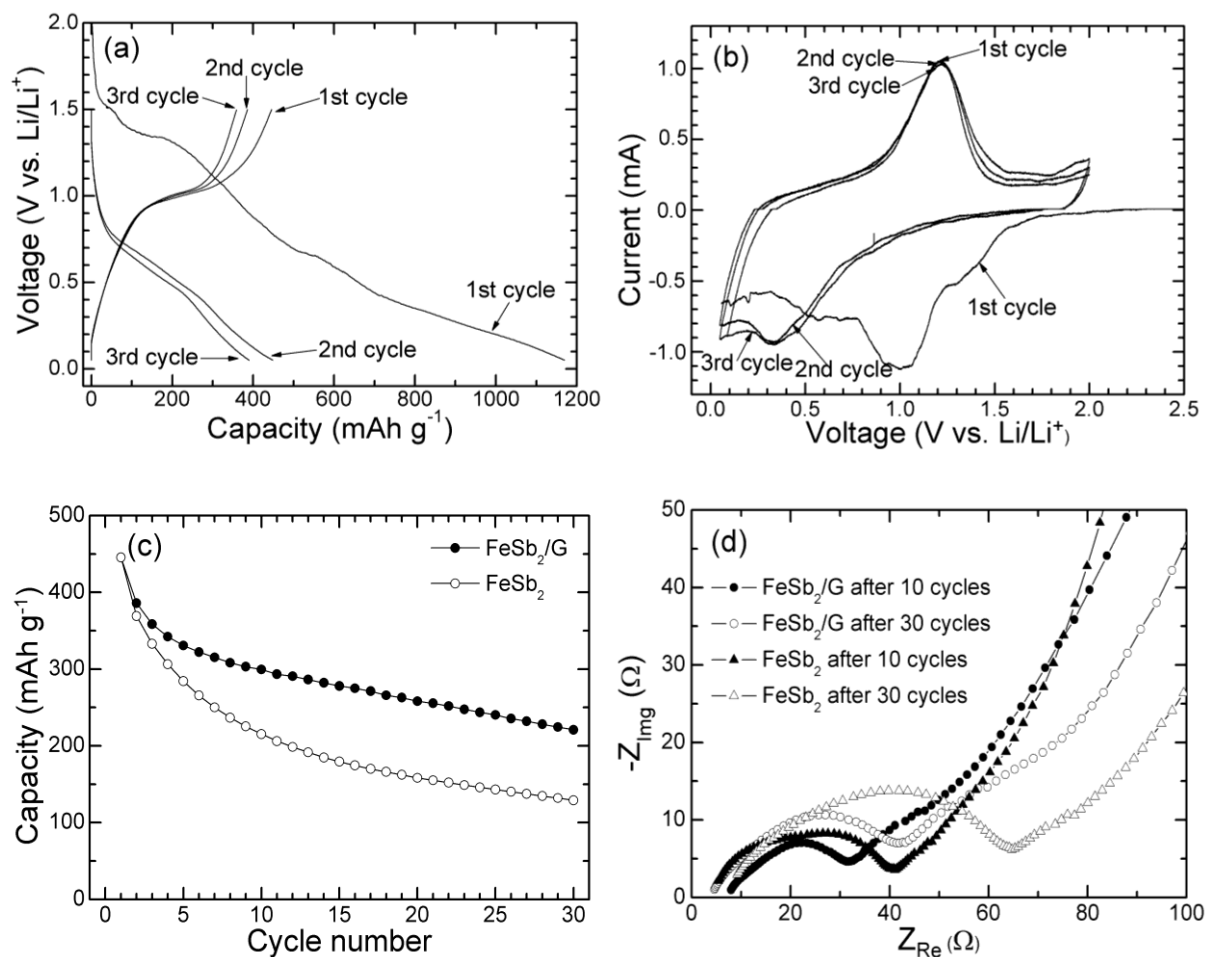
Figure 4. Charge-discharge curves (a) and CV (b) plots of $FeSb_2/G$, (c) comparison of cycling stability between $FeSb_2/G$ and bare $FeSb_2$, and (d) Nyquist plots of $FeSb_2/G$ and $FeSb_2$ after different cycles.

4. CONCLUSIONS

In summary, layered $NiSb/G$ and $FeSb_2/G$ nanocomposites have been successfully synthesized by one-step in situ solvothermal route. The formation of the $NiSb$ and $FeSb_2$ alloys occurs simultaneously with the reduction of GO to graphene. The interaction between the precursors plays an important role in the microstructure of the alloy nanoparticles. The nanosized $NiSb$ and $FeSb_2$ particles are uniformly dispersed and firmly confined by the graphene sheets. The electrochemical tests show

that the electrochemical performance of the alloy nanoparticles can be improved by loading them in between the graphene sheets due to the confining, buffering and conducting effects of graphene.

References

1. R. Alcántara, F. J. Fernández-Madrigal, P. Lavela, J. L. Tirado, J. C. Jumas, and J. Olivier-Fourcade, *J. Mater. Chem.* 9 (1999) 2517.
2. D. Larcher, L. Y. Beaulieu, O. Mao, A. E. George, and J. R. Dahn, *J. Electrochem. Soc.* 147 (2000) 1703.
3. L. J. Zhang, X. B. Zhao, X. B. Jiang, C. P. Lv, and G. S. Cao, *J. Power Sources* 94 (2001) 92.
4. M. Wachtler, M. Winter, and J. O. Besenhard, *J. Power Sources* 105 (2002) 151.
5. L. Monconduit, J. C. Jumas, R. Alcántara, J. L. Tiradob, and C. Pérez Vicente, *J. Power Sources* 107 (2002) 74.
6. H. Honda, H. Sakaguchi, I. Tanaka, and T. Esaka, *J. Power Sources* 123 (2003) 216.
7. J. Santos Peña, J. Cuart Pascual, A. Caballero, J. Moralesa, and L. Sánchez, *J. Solid State Chem.* 177 (2004) 2920.
8. C. Villevieille, C. M. Ionica-Bousquet, B. Ducourant, J. C. Jumas, and L. Monconduit, *J. Power Sources* 172 (2007) 388.
9. M. Stjerndahl, H. Bryngelsson, T. Gustafsson, J. T. Vaughey, M. M. Thackeray, and K. Edström, *Electrochim. Acta* 52 (2007) 4947.
10. S. Matsuno, M. Noji, T. Kashiwagi, M. Nakayama, and M. Wakihara, *J. Phys. Chem. C* 111 (2007) 7548.
11. S. Matsuno, M. Nakayama, and M. Wakihara, *J. Electrochem. Soc.* 155 (2008) A61.
12. X. M. Zheng, Y. Xiao, L. Huang, F. S. Ke, Y. He, J. T. Li, G. Z Wei, and S. G. Sun, *Electrochem. Commun.* 11 (2009) 1803.
13. S. W. Song, R. P. Reade, E. J. Cairns, J. T. Vaughey, M. M. Thackeray, and K. A. Striebel, *J. Electrochem. Soc.* 151 (2004) A1012.
14. V. Pralong, J. B. Leriche, B. Beaudoin, E. Naudin, M. Morcrette, and J. M. Tarascon, *Solid State Ionics* 166 (2004) 295.
15. H. Bryngelsson, J. Eskhult, L. Nyholm, and K. Edström, *Electrochim. Acta* 53 (2008) 7226.
16. M. Z. Xue and Z. W. Fu, *Electrochem. Commun.* 8 (2006)1250.
17. P. Limthongkul, H. F. Wang, and Y. M. Chiang, *Chem. Mater.* 13 (2001) 2397.
18. T. Sarakonsri, C. S. Johnson, S. A. Hackney, and M. M. Thackeray, *J. Power Sources* 153 (2006) 319.
19. J. Moralesa, L. Sánchez, F. Martín, and F. Berry, *J. Solid State Chem.* 179 (2006) 2554.
20. J. Cho and S. Lim, *J. Electrochem. Soc.* 155 (2008) A825.
21. H. Kim and J. Cho, *Chem. Mater.* 20 (2008) 1679.
22. J. Xie, G. S. Cao, X. B. Zhao, Y. D. Zhong, and M. J. Zhao, *J. Electrochem. Soc.* 151 (2004) A1905.
23. J. Xie, X. B. Zhao, G. S. Cao, M. J. Zhao, and S. F. Su, *J. Power Sources* 140 (2005) 350.

24. J. Xie, X. B. Zhao, G. S. Cao, J. L. Mi, J. Tu, H. Y. Qin, G. S. Cao, and J. P. Tu, *Electrochem. Solid-State Lett.* 9 (2006) A336.
25. W. X. Chen, J. Y. Lee, and Z. L. Liu, *Carbon* 41 (2003) 959.
26. J. Xie, X. B. Zhao, G. S. Cao, and M. J. Zhao, *Electrochim. Acta* 50 (2005) 2725.
27. J. X. Zhu, T. Sun, J. S. Chen, W. H. Shi, X. J. Zhang, X. W. Lou, S. Mhaisalkar, H. H. Hng, F. Boey, J. Ma, and Q. Y. Yan, *Chem. Mater.* 22 (2010) 5333.
28. J. Hassoun, G. Derrien, S. Panero, and B. Scrosati, *J. Power Sources* 183 (2008) 339.
29. C. M. Park and H. J. Sohn, *Chem. Mater.* 20 (2008) 3169.
30. C.M. Park and H.J. Sohn, *J. Electrochem. Soc.* 157 (2010) A46.
31. K. S. Novoselov, A. K. Geim, S. V. Morozov, D. Jiang, Y. Zhang, S. V. Dubonos, I. V. Grigorieva, and A. A. Firsov, *Science* 306 (2004) 666.
32. S. Park, J. H. An, I. W. Jung, R. D. Piner, S. J. An, X. S. Li, A. Velamakanni, and R. S. Ruoff, *Nano Lett.* 9 (2009) 1593.
33. M. D. Stoller, S. Park, Y. W. Zhu, J. H. An, and R. S. Ruoff, *Nano Lett.* 8 (2008) 3498.
34. C. Lee, X. D. Wei, J. W. Kysar, and J. Hone, *Science* 321 (2008) 385.
35. G. X. Wang, B. Wang, X. L. Wang, J. Park, S. X. Dou, H. Ahn, and K. Kim, *J. Mater. Chem.* 19 (2009) 8378.
36. J. K. Lee, K. B. Smith, C. M. Hayner, and H. H. Kung, *Chem. Commun.* 46 (2010) 2025.
37. S. L. Chou, J. Z. Wang, M. Choucair, H. K. Liu, J. A. Stride, and S. X. Dou, *Electrochem. Commun.* 12 (2010) 303.
38. S. Q. Chen, P. Chen, M. H. Wu, D. Y. Pan, and Y. Wang, *Electrochem. Commun.* 12 (2010) 1302.
39. S. M. Paek, E. Yoo, and I. Honma, *Nano Lett.* 9 (2009) 72.
40. J. Yao, X. P. Shen, B. Wang, H. K. Liu, and G. X. Wang, *Electrochem. Commun.* 11 (2009) 1849.
41. L. S. Zhang, L. Y. Jiang, H. J. Yan, W. D. Wang, W. Wang, W. G. Song, Y. G. Guo, and L. J. Wan, *J. Mater. Chem.* 20 (2010) 5462.
42. D. H. Wang, R. Kou, D. W. Choi, Z. G. Yang, Z. M. Nie, J. Li, L. V. Saraf, D. H. Hu, J. G. Zhang, G. L. Graff, J. Liu, M. A. Pope, and I. A. Aksay, *ACS Nano* 4 (2010) 1587.
43. W. S. Hummers and R. E. Offeman, *J. Am. Chem. Soc.* 80 (1958) 1339.
44. D. Li, M. B. Müller, S. Gilje, R. B. Kaner, and G. G. Wallace, *Nat. Nanotechnol.* 3 (2008) 101.
45. S. Stankovich, D. A. Dikin, R. D. Piner, K. A. Kohlhaas, A. Kleinhammes, Y. Y. Jia, Y. Wu, S. T. Nguyen, and R. S. Ruoff, *Carbon* 45 (2007) 1558.
46. Z. T. Deng, F. Q. Tang, D. Chen, X. W. Meng, L. Cao, B. S. Zou, *J. Phys. Chem. B* 110 (2006) 18225.
47. S. Stankovich, R. D. Piner, X. Q. Chen, N. Q. Wu, S. T. Nguyen, and R. S. Ruoff, *J. Mater. Chem.* 16 (2006) 155.
48. L. Zhang, Y. Li, L. Zhang, D. W. Li, D. Karpuzov, Y. T. Long, *Int. J. Electrochem. Sci.* 6 (2011) 819.
49. D. Aurbach, *J. Power Sources* 89 (2000) 206.